Full Length Article

Synergistic combination of nanostructured sodium metal anode and capacitive cathode for advanced non-aqueous hybrid capacitors

Sunwoo Park[a,1], Jong Chan Hyun[b,1], Jin Hwan Kwak[c], Min Eui Lee[d], Hyoung-Joon Jin[a,*], Young Soo Yun[b,*]

[a] Department of Polymer Science and Engineering, Inha University, Incheon 22212, South Korea
[b] KU-KIST Graduate School of Converging Science and Technology, Korea University, 145 Anam-ro, Seongbuk-gu, Seoul 02841, South Korea
[c] Department of Chemical Engineering, Kangwon National University, Samcheok 245-711, South Korea
[d] Carbon Composite Materials Research Center, Institute of Advanced Composite Materials, Korea Institute of Science and Technology, 92 Chudong-ro, Bongdong-eup, Wanju-gun, Jeollabuk-do 55324, South Korea

ABSTRACT

Sodium metal hybrid capacitors (SMHCs) are a new type of energy storage device (ESD) composed of metal anodes and capacitive cathodes. In this study, an SMHC consisting of a nanostructure-engineered pyropolymer electrode pair is fabricated, which exhibits significantly high specific power and energy and exceptionally long lifetime. The critical obstacles of metal anodes such as the low Coulombic efficiencies (CEs) and safety problems originating from the dendritic metal growth are overcome using a stereoscopic pyropolymer thin layer including multitudinous sodiophilic sites, which can function as both electrolyte-intimate spot and nucleation catalyst. The well-designed metal anode exhibits a remarkably high average CE of ~99.95%, high rate capabilities up to 4 mA cm^{-2}, and stable cycling over 1000 cycles. In addition, the nanopore-controlled pyropolymer containing nanopores with diameters mainly of ~2 nm exhibits outstanding rate capabilities with a capacity retention of ~60% of the initial capacity at a high current rate of ~50 A g^{-1} in a cathodic voltage region of 1.0–4.2 V in a diglyme-based electrolyte. The nanostructure-engineered pyropolymer-based electrodes are assembled as a pair of Faradic and non-Faradic electrodes in an SMHC, which exhibits the highest specific power of ~85,300 W kg^{-1} at 143.3 W h kg^{-1} and specific energy of ~347.7 W h kg^{-1} at 1241.8 W kg^{-1} among those of the reported sodium-based ESDs. Considering the simple chemistry, cheap components, and mass-producible process, the high-performance SMHC is a very promising device for use as a power source in electric vehicles and large-scale ESDs.

1. Introduction

Non-aqueous alkali-ion hybrid capacitors (AIHCs), such as the Li- and Na-ion hybrid capacitors, are hybrid types of energy storage device consisting of pairs of typical capacitive and Faradic electrodes as asymmetric configurations [1–5]. The combined electrode system has been proposed to achieve high supercapacitor-like power and high rechargeable-battery-like energy density. However, the kinetic and energy imbalances between the different types of electrode lead to significant energy losses and low rate capabilities, which hinder the applications of AIHCs [6–10]. In a Faradic electrode, the charge transport rate of conventional active host materials based on an intercalation reaction is limited by the poor solid-state-diffusion kinetics of the guest ions, which is several orders of magnitude lower than that of

the surface-driven physisorption on the capacitive electrode [11,12]. Although the diffusion rate can be improved by reducing the charge delivery pathway through a nanostructured design, the active nano-materials lead to other critical obstacles such as the large irreversible side reaction and absence of plateau capacity, and thus to a critical loss in energy density [13–15]. Alternatively, high-rate active materials based on intercalation pseudocapacitance and cointercalation have been developed as Faradic electrodes [16–19]. These types of host materials can accept solvated charges very quickly in their internal active sites, leading to well-balanced kinetic performances with the capacitive electrode counterpart. Nevertheless, the high-rate materials with insufficient capacities and operation voltages have yet to provide large improvements in energy densities compared with those of electrochemical double-layer capacitors. Therefore, a new type of high-
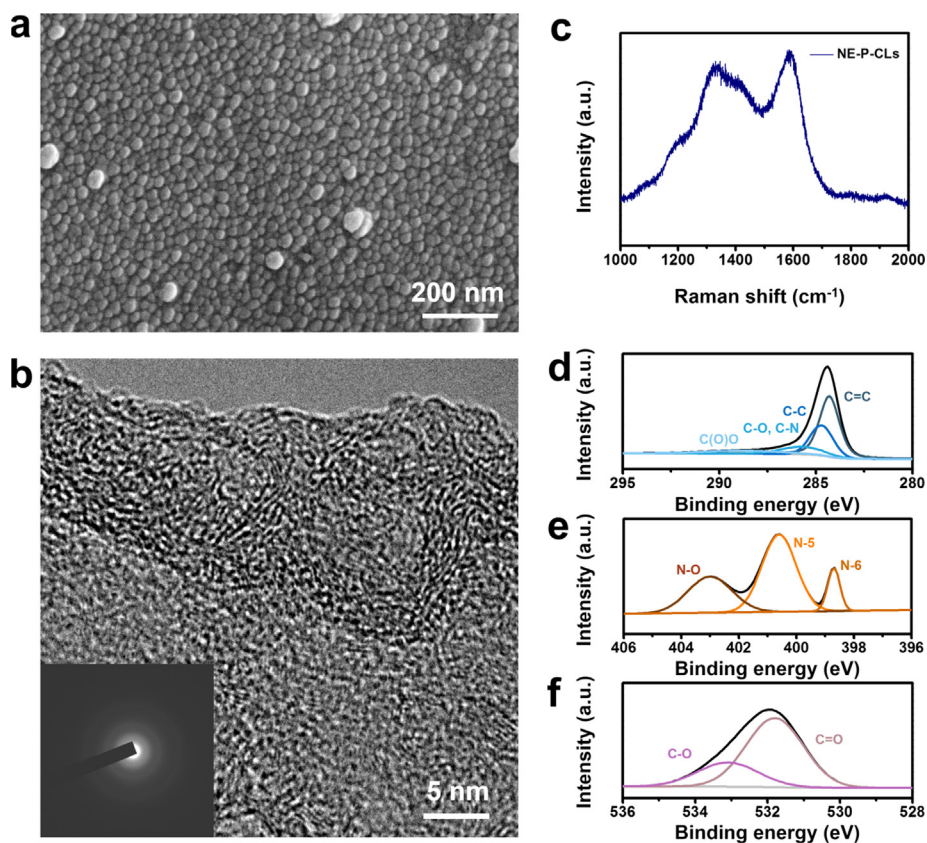
Fig. 1. Material properties of NE-P-CL. (a) FESEM and (b) FETEM images (inset: selected-area electron diffraction pattern), (c) Raman spectrum, and (d) C 1*s*, (e) N 1*s*, and (f) O 1*s* XPS spectra.

performance Faradic electrode is required for the hybrid energy storage system.

The sodium metal anode (SMA) has attracted large interest as the Faradic electrode, because of its high theoretical capacity of ~1166 mA h g^{-1}, low redox potential of -2.71 V vs. standard hydrogen electrode, and abundant sodium resources in the nature [20–23]. Although the SMA suffers from a low Coulombic efficiency (CE) and safety issues owing to the dendritic metal growth, these obstacles have been addressed by extensive studies [20–30]. In particular, the use of a catalytic carbon layer with a glyme-based electrolyte is highly effective to mitigate the dendritic metal growth [21,23]. The sodiophilic carbon layer with a large active surface area enabled a rapid metal deposition/dissolution (at ~4 mA cm^{-2}), while the glyme-based electrolyte effectively provided stable cycling loops with a high average CE over 99.9%, yielding considerably high rate performances, large cycling lifetimes over 1000 cycles, and high energy densities [21,23]. Therefore, the SMAs are promising Faradic electrodes for a new type of energy storage device, sodium metal hybrid capacitors (SMHCs), which could be more practicable with the use of a well-engineered and nanostructured material obtained by a simple fabrication.

Activated carbons (ACs) with microporous structures are well-known capacitive electrodes for AIHCs, because of their large specific surface areas, good intra- and interparticle electrical conductivities, electrolyte accessibility, simple chemistry, and mass scalability [2]. In a conventional carbonate-based electrolyte, they can deliver specific capacities of approximately 50–100 mA h g^{-1} [1,5]. The specific capacities can be increased by expanding the operation voltage window into the more anodic voltage range below the open-circuit voltage (OCV) by *amphi*-charge storage effects [31]. However, the pseudocapacitive alkali cation storage exhibits a large voltage hysteresis between charge and discharge profiles, leading to a low energy efficiency [31–33]. In addition, the relatively low kinetic performance of chemisorption can

reduce the rate capabilities of the capacitive electrode. The charge storage behaviors of ACs are dependent on the solvent system, owing to the different solvation energies according to the solvent molecules [34–36]. Kang et al. reported that linear ethers such as diethylene glycol dimethyl ether (DEGDME) strongly solvate Na ions because they contain multiple oxygen atoms in their structures, which can simultaneously stabilize the Na ions [36]. The higher desolvation energies of the Na-ion–DEGDME complexes than those of carbonate-based Na-ion complexes could hinder the pseudocapacitive behaviors in the voltage region below the OCV, leading to a different charge storage mechanism. However, in contrast to the well-established charge storage behaviors of ACs in a carbonate-based electrolyte, their electrochemical performances in the ether-based electrolyte system are not well understood.

In this study, we designed a new type of high-power SMA based on a nanoembossing pyropolymer catalytic layer (NE-P-CL) coated on a Cu foil. Pyropolymer is a highly functionalized carbonaceous material obtained using a polymer precursor upon a simple heating process [31]. The pyropolymer material properties can be largely tuned according to the precursor polymer and pyrolysis conditions. We designed NE-P-CL using a nitrogen-rich polyvinylpyrrolidone (PVP) by spin coating and following low-temperature heating. The resulting NE-P-CL had a large number of sodiophilic sites and stereoscopic morphology, providing stable sodium metal deposition/dissolution cycling behaviors with CEs of almost 100% in a wide current rate range of 0.5 to 4.0 mA cm^{-2}. In addition, as a high-performance counterpart electrode, a nanopore-engineered pyropolymer (NE-PP) composed mostly of ~2-nm pores was fabricated by a controlled heating process. In a diglyme-based electrolyte, NE-PP exhibited high electrochemical performances, particularly rate capabilities in the range of 0.5–50 A g^{-1}. The nanostructured pyropolymer electrode pair was used to fabricate an SMHC having considerably high electrochemical performances including a specific power of ~85,300 W kg^{-1} at 143.3 W h kg^{-1} and specific energy of
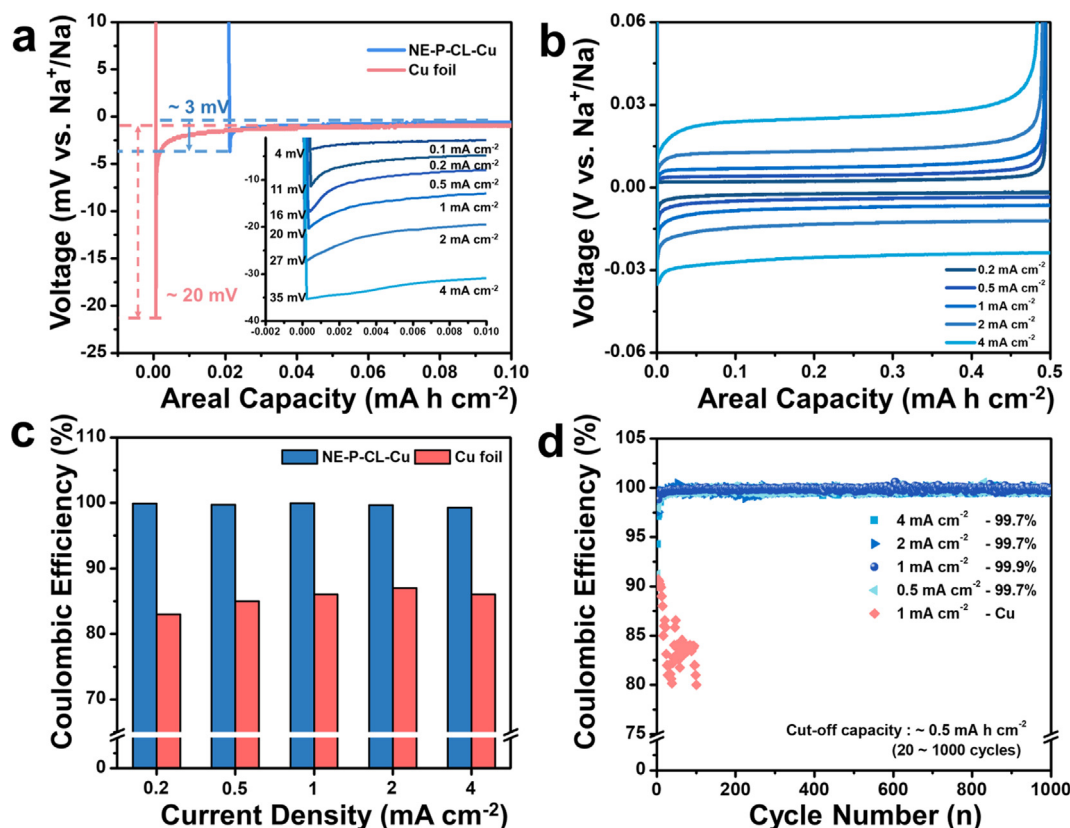
Fig. 2. Electrochemical sodium metal deposition/dissolution performances of the NE-P-CL-based anode characterized with a cut-off capacity of 0.5 mA h cm^{-2}. (a) Galvanostatic sodium metal deposition profiles of the NE-P-CL- and Cu-foil-based anodes at 0.05 mA cm^{-2} (inset: initial discharge profiles of the NE-P-CL-based anode at different current densities), (b) galvanostatic sodium metal deposition/dissolution profiles of the NE-P-CL-based anode at different current densities, (c) current rate–CE bar graph of both NE-P-CL- and Cu-foil-based anodes at different current densities, and (d) Sodium metal deposition/dissolution cycling behaviors of the NE-P-CL-based anode over 1000 cycles at different current densities and Cu-foil-based anode at 1 mA cm^{-2} over 100 cycles.

~347.7 W h kg^{-1} at 1241.8 W kg^{-1}, with a long-term cycling stability over 1000 cycles.

2. Results and discussion

A smooth PVP layer approximately 1 μm thick was spin-coated onto a Cu foil, as shown in Fig. S1(a, b). With the increase in heating temperature, the thin film melted in the temperature range of 150–200 °C, yielding a very rough surface, which could be attributed to the poor interaction between the PVP melt and Cu substrate (Fig. S1(c–e)). The following pyrolysis of the PVP melt at 600 °C provided a rougher surface topology, where a stereoscopic nanostructure with semicircle nanoprotuberances embossed on the surface was eventually formed, as shown in the field-emission scanning electron microscopy (FESEM) image of NE-P-CL (Fig. 1(a)). In contrast to the considerable change in microscopic topology, the macroscopic photograph of NE-P-CL coated on the Cu foil shows only a slight color change to darker brown, compared with the bare Cu foil (Fig. S2). To characterize the microstructure of NE-P-CL using transmission electron microscopy (TEM), the Cu foil was removed in a 0.1-M ammonium persulfate solution and the floated NE-P-CL was mounted on a holey TEM grid (Fig. S3). The high-resolution TEM image shows an amorphous structure without a long-range ordering (Fig. 1(b)). The inset selected-area electron diffraction pattern confirms the amorphous carbon microstructure. The Raman spectrum further supports the TEM results, where very broad and fused D and G bands are observed (Fig. 1(c)). The D and G bands originate from the disorder in the A_{1g} breathing mode of the six-membered aromatic ring near the basal edge and hexagonal structure related to the E_{2g} vibration mode of the sp^2-hybridized carbon atoms, respectively [37]. The similar D and G intensities suggest that the defective sp^2

carbon domain has in-plane dimensions of a few nanometers.

The chemical structure of NE-P-CL is investigated by X-ray photoelectron spectroscopy (XPS) (Fig. 1(d–f)). In the deconvoluted C 1s spectrum, a large sp^2 carbon–carbon double bonding peak is observed at 284.4 eV (Fig. 1(d)). In addition, distinct sp^3 carbon–carbon bonding and carbon–nitrogen/carbon–oxygen bonding structures are observed at 284.7 and 285.9 eV, respectively. The nitrogen groups are composed of three different structures, pyridinic-N, pyridonic-N, and N-oxide, having peaks centered at 398.7, 400.6, and 403.0 eV, respectively (Fig. 1(e)). The oxygen groups are present mainly as carbon–oxygen single and double bonding configurations, with peaks at 533.1 and 531.8 eV, respectively (Fig. 1(f)). The calculated atomic ratios of oxygen and nitrogen to carbon (C/O and C/N ratios) are 5.7 and 19.4, respectively. These results indicate that NE-P-CL has a large number of extrinsic defects in the carbon structure, which can be sodiophilic catalytic sites guiding a homogeneous metal deposition [38]. The formation of a defective carbon structure is a plausible result, because is obtained by a relatively low temperature pyrolysis (< 1000 °C) of a polymer precursor. PPs have large numbers of intrinsic carbon defects such as Stone–Wales, mono-/di-vacancy, and edge defects as well as extrinsic defects, which distort the planar polyhexagonal carbon structure into irregular three-dimensional shapes. Therefore, the highly amorphous and complex disordered structure is a characteristic microstructure of the PP-based NE-P-CL. As the sodium ion can penetrate the amorphous carbon structure, the defect sites of NE-P-CL can be a redox host in the anodic voltage region. The sodium-ion storage capacity of the amorphous carbon is approximately 300 mA h g^{-1}, which corresponds to Na$_{0.8}$C$_6$ and ~0.26 M$_{sodium}$ g^{-1} [39,40]. If the NE-P-CL loading mass is ~0.01 mg, the calculated content of active catalytic sites is approximately 1.57×10^{18} ea. The considerable augmentation

of metal nucleation sites could enable kinetically controlled metal deposition, providing homogeneous (film-like) metal deposition/striping cycles. In addition, the numerous nanoscale trenches formed by the stereoscopic morphology can act as an electrolyte reservoir, supplying sodium ions immediately to the subcontiguous metal nucleation sites. Fig. S4 shows contact angle images of electrolyte droplets on the surfaces of NE-P-CL and Cu foil. Upon the contact with the surface, the droplet permeated into NE-P-CL, indicating a high affinity (Fig. S4(a)). In contrast, on the surface of the Cu foil, the electrolyte droplet exhibited a contact angle of 52.8°, indicating a low wettability (Fig. S4(b)).

The electrochemical performances of NE-P-CL coated on the Cu foil for a sodium metal deposition/dissolution cycling were evaluated in an electrolyte of 1 M of $NaPF_6$ dissolved in DEGDME with a cut-off capacity of 0.5 mA h cm^{-2} (Fig. 2). In the galvanostatic discharge profile at a current density of 0.05 mA cm^{-2}, the NE-P-CL-based anode exhibited a voltage overshooting (VO) of ~3 mV in the early stage of metal deposition, approximately seven times lower than that (~20 mV) of the bare Cu-foil-based anode (Fig. 2(a) and Fig. S5). The VO originates from the nucleation overpotential of metal seeds, which can be conventionally construed by the relationship between the thermodynamic nucleation energy and spherical nucleus radius, as shown by the equation for homogeneous nucleation, $\Delta G_{nucleation} = -4/3\pi r^3 \Delta G_V + 4\pi r^2 \Upsilon$, where $\Delta G_{nucleation}$ is the Gibbs energy for the formation of a spherical nucleus having a radius of r, ΔG_V is the free energy change per volume, and Υ is the surface energy of the Na–electrolyte interface [41,42]. In the electrochemical system at a given current density, the nucleus size is governed by the kinetic conditions, leading to a change in critical nucleus size. The interrelation between the overpotential and critical nucleus radius was reported by Pei et al., who demonstrated the cubic relationship between the areal nuclei density and critical nucleus radius [43]. According to the reported results, the large increase in content of catalytic nucleation sites could induce an infinite decrease in critical nucleus size, leading to a very large increase in overpotential. However, unlike the expectation, NE-P-CL including numerous nucleation sites significantly reduces the nucleation overpotential. In addition, a homogeneous metal deposition as a film-like shape is observed in the ex-situ SEM characterization with different cut-off capacities of 0.5, 1.0 and 1.5 mA h cm^{-2} at different current densities of 1.0 and 2.0 mA cm^{-2} (Fig. S6). Morphologies of the deposited metals are clearly differentiated from them with dendrite-like shapes on Cu foil-based anode (Fig. S7). These results suggest that the metal nucleation and growth on the NE-P-CL-based anode proceed in a different manner from that of the conventional nucleus theory that presupposes a (semi)spherical-particle-shape growth. Wang et al. reported that a high-lithium-ion-affinity sponge can lead to a higher local concentration of Li ions in the interfacial area than in the bulk solution, which promotes their electrokinetic surface conduction and electro-osmosis during Li plating/stripping [44,45]. The improved Li ion transport capability effectively reduces the concentration polarization and overcomes the diffusion-limited current, enabling a uniform Li-ion distribution. NE-P-CL also has a high sodium ion affinity, owing to the large numbers of sodiophilic heteroatoms. Therefore, there is a high probability that NE-P-CL guides a film-like sodium metal growth along with its sodiophilic surface rather than a spherical particle shape. Therefore, it is likely that the deposited metal on NE-P-CL is homogeneously coated on the carbon layers, which then grow as a bulk-film-like shape minimizing the surface energy (Υ). In the homogeneous coating model, $\Delta G_{nucleation}$ is dependent mainly on ΔG_V as a negative value, leading to the lower nucleation overpotential. In addition, when the current rate is systematically increased to 0.1, 0.2, 0.5, 1.0, 2.0, and 4.0 mA cm^{-2}, the minimum voltage peak gradually decreases to -4, -11, -16, -20, -27, and -35 mV, respectively. The large change in overpotential with the current rate originates from the reduction in Ohmic polarization rather than from the metal nucleation overpotential. As shown in Fig. 2(b), the voltage hysteresis of the plateaus between the discharge

and charge profiles increases with the current rate, while the VO is not considerably changed (inset of Fig. 2(a)). This result supports the claim that the gradual increase in polarization with the current rate originates mainly from Ohmic drops. In contrast, the lowest voltage peak (-35 mV) at the 80 times higher current rate (4.0 mA cm^{-2}) than the initial value (0.05 mA cm^{-2}) still corresponds to a very low polarization. This implies that, at the higher current rate, the sodium metal deposition kinetics are slightly affected, which can maintain the kinetically controlled metal deposition.

A significant result is observed in the current rate–CE graph (Fig. 2(c)). In the galvanostatic sodium metal plating/striping cycles (20th–100th), the NE-P-CL-based anode exhibited considerably high average CE values, affected by the current rate. In particular, the highest CE of ~99.95% was observed at the current density of 1.0 mA cm^{-2}. The CE slightly decreased with the increase in current rate; a CE of 99.7% was achieved at 4.0 mA cm^{-2}, indicating the high rate-cycling performances (Fig. 2(c)). In contrast, the bare Cu-foil-based anode exhibited low CEs of 83–87% at all current rates (Fig. 2(d)). Further, the specific cycling performances of the NE-P-CL-based anode were evaluated over 1000 cycles at a current rate of 1.0 mA cm^{-2} with a cut-off capacity of 0.5 mA h cm^{-2} (Fig. 2(d)). In the consecutive cycling, NE-P-CL–Cu maintained the highly stable metal deposition/dissolution cycles with an average CE of ~99.9% in the 20th–1000th cycles (Fig. 2(d)). At 1000th cycle under 1 mA cm^{-2}, the galvanostatic discharge profile of NE-P-CL-based anode shows VO of ~9 mV which is still below half of the initial VO value of the Cu-based anode at 0.05 mA cm^{-2}, and its plateau overpotential is below 8 mV (Fig. S8). In addition, the voltage hysteresis between discharge/charge profiles at 1000th cycle was maintained as ~15 mV (Fig. S8). We further confirmed the cycling performances of NE-P-CL-based anode in symmetric devices characterized at different current densities (Fig. S9). The cycle number vs. voltage curves of symmetric devices exhibit stable cycling behaviors during 1200 cycles at different current densities of 1.0, 2.0 and 4.0 mA cm^{-2}, demonstrating great cycling performances. The stable cycling could be attributed to the dendrite-free film-like metal deposition behaviors on the sodiophilic NE-P-CL. The XRD pattern obtained after 1000 repetitive cycling process exhibited no sodium metal peak, indicating that there was no sodium metal-based byproduct originating from dendritic metal growth (Fig. S10). In contrast, a clear sodium metal peak was observed after the subsequent sodium metal deposition process, indicating a reversible sodium metal deposition/stripping cycling process (Fig. S10). Hence, the results suggest dendritic metal-free cycling behaviors of the sodiophilic NE-P-CL. To confirm the heteroatom effects on the electrochemical performances, NE-P-CL was further heated at 800 °C under H_2 atmosphere, and electrochemical performances of the H_2-treated NE-P-CL (H-NE-P-CL)-based anode were tested (Fig. S11). The H-NE-P-CL-based anodes showed higher VO values in all the current densities from 0.2 to 4 mA cm^{-2} than values of NE-P-CL-based anodes in the galvanostatic discharge profiles, indicating relatively poor catalytic effects (Fig. S11(a, b)). In addition, CE values of H-NE-P-CL-based anodes are lower than those of NE-P-CLs, and their CEs sharply decreased at 4 mA cm^{-2} (Fig. S11(c)). Moreover, the H-NE-P-CL-based anode showed relatively low CE values corresponding to ~99.6% during cycling tests (Fig. S11(d)). These results demonstrate that the heteroatom-rich NE-P-CLs are more useful as a catalytic sodium metal anode. Additionally, the surface-driven charge-storage behaviors of NE-P-CLs were tested in the voltage range of 0.01–2.7 V vs. Na^+/Na under a galvanostatic discharge/charge process (Fig. S12). Because the NE-P-CL was a thin film, the areal capacity was ~2 μA h cm^{-2}, indicating that the capacitive charge-storage capacity was insignificant.

As capacitive electrodes, NE-PPs were prepared using waste green tea (WGT) by controlled pyrolysis and activation, as illustrated in Fig. S13. The contents of activation agents considerably affected their pore structures (Fig. 3(a), Table 1). The fabricated NE-PPs are denoted as 4-NE-PP, 6-NE-PP, and 8-NE-PP, having KOH contents of 400, 600, and
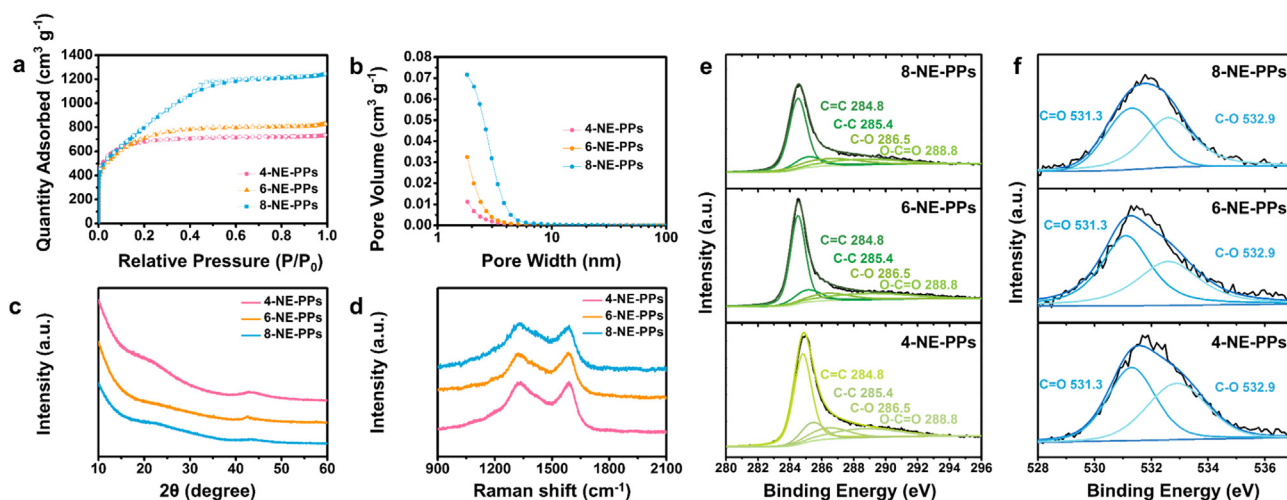
Fig. 3. Material properties of NE-PPs. (a) Nitrogen adsorption/desorption isotherms, (b) pore size distributions, (c) XRD patterns, (d) Raman spectra, and (e) C 1s and (f) O 1s XPS spectra.

Table 1
Textural properties of NE-PPs and C-AC.

Sample	$^{a}S_{BET}$	$^{b}V_{Tot}$	$^{c}S_{Mic}$	$^{d}S_{Meso}$	$^{e}V_{Mic}$	^{f}APS	^{g}APR
4-NE-PP	2491.4	1.1	2299.6	191.8	0.98	18.3	4.1
6-NE-PP	2577.3	1.3	2082.4	494.9	0.92	19.9	5.1
8-NE-PP	2939.9	1.9	101.6	2838.3	0.04	26.2	6.4
C-AC	1692.5	0.8	1618.4	74.1	0.67	18.3	3.7

^{a} Brunauer–Emmett–Teller surface area ($m^2 \ g^{-1}$).
^{b} Total pore volume ($cm^3 \ g^{-1}$).
^{c} Micropore surface area ($m^2 \ g^{-1}$).
^{d} Mesopore surface area ($m^2 \ g^{-1}$).
^{e} Micropore volume ($cm^3 \ g^{-1}$).
^{f} Average particle size (Å).
^{g} Average pore radius (V/A) (Å).

800% with respect to the WGT, respectively. Activation of the polymeric precursor with KOH occurs via two main mechanisms. The first step is the consumption of carbon by oxygen, which is catalyzed by alkali metals below 700 °C, producing carbon monoxide and carbon dioxide. The second activation mechanism occurs above 700 °C and is accompanied by the formation of metallic potassium. This metallic potassium penetrates the graphitic layers formed by pyrolysis and results in numerous topological defects and the expansion of the graphitic lattice via the rapid removal of the intercalated potassium. We found that the porous structure of carbon materials can be tuned by changing the KOH content.[31] However, when excessive KOH is used, a large amount of carbon is consumed in the first step, resulting in a poor yield. Therefore, an engineering process is crucial for developing nanopores in the resulting carbon materials. In this study, the optimal KOH contents were determined to be 400–800% (relative to the precursor material). The nitrogen adsorption and desorption isotherms of 4-NE-PP show a large increase in nitrogen adsorption at relative pressures (RPs) smaller than 0.01, followed by a plateau and low adsorption in the RP range above 0.2. The isotherm shape indicates a typical International Union of Pure and Applied Chemistry (IUPAC)-type-I microporous structure. The monolayer adsorption of nitrogen molecules occurs in the lower-RP region (< 0.01) on the open surface. The following multilayer adsorption of nitrogen molecules in the pores with sizes of 2–50 nm leads to pore filling, yielding hysteresis between the adsorption and desorption isotherms. However, unlike the typical mesopore-filling behaviors, the isotherms of NE-PPs exhibit distinctive changes without hysteresis in the RP range of 0.01–0.4. In particular, the isotherm of 8-NE-PP shows a very large increase in nitrogen adsorption at an RP of 0.5, with an insignificant hysteresis. The change in the isotherm is

closely related to the pore size alteration, as shown in Fig. 3(b). The pore size distribution of NE-PP is shifted into the larger-pore-diameter region with the addition of activation agents. 8-NE-PP has few nanometers larger pore sizes than those of 4-NE-PP and 6-NE-PP. Nevertheless, the pore sizes of 8-NE-PP are still mainly ~2 nm; most of them are smaller than 4 nm. The increase in few-nanometer pore content could lead to a change in the isotherm, differentiating it from the typical isotherms observed for mesoporous structures. Specific textural properties of NE-PPs and commercial activated carbons (C-ACs) are shown in Table 1.

Contrary to the large differences in pore structures, the carbon microstructures of NE-PPs are similar. The X-ray diffraction (XRD) patterns are similar with no distinct peaks (Fig. 3(c)), indicating the amorphous carbon structures. The high-resolution FETEM images of NE-PPs further confirm the amorphous structures without long-range graphitic ordering (Fig. S14). The Raman spectra of NE-PPs are also similar with broad and fused D and G bands (Fig. 3(d)). The D to G intensity ratio (I_D/I_G) is approximately 1.0. The D and G bands indicate that NE-PPs are composed of polyhexagonal sp^2 carbon structures. The I_D/I_G value close to 1.0 suggests that the polyaromatic ring structure has a domain size of a few nanometers. The surface properties of NE-PPs were characterized by XPS. In the deconvoluted C 1s spectra, signals of several chemical structures such as sp^2 and sp^3 carbon bondings and carbon–oxygen bonding groups are observed (Fig. 3(e)). The deconvoluted O 1s spectra show two broad peaks of the carbon–oxygen single and double bonding groups (Fig. 3(f)). The C/O ratios of NE-PPs are 11.0–11.5. The XPS data demonstrate that NE-PPs have similar surface properties including oxygen functional groups. The hydrophilic functional groups could lead to a better wettability of the electrolyte and improved quantum capacitance.

The electrochemical performances of NE-PPs were evaluated in an electrolyte of 1 M of $NaPF_6$ dissolved in DEGDME in a voltage window of 1.0–4.2 V vs. Na^+/Na (Fig. 4). Because the DEGDME-based electrolyte system is optimal with regard to the electrochemical performance of the SMA anode, it is used for the cathode part. The galvanostatic charge/discharge profiles of NE-PPs are linear in the operation voltage window, with a small voltage hysteresis between the charge and discharge curves. The capacitive charge storage behaviors are similar for all samples, while their specific capacities are considerably different (Fig. 4(a–c)). 8-NE-PP exhibits a specific capacity of 156 mA h g^{-1} at a specific current rate of 0.5 A g^{-1} (Fig. 4(c)), while 4- and 6-NE-PPs exhibit specific capacities of 95 and 101 mA h g^{-1} (Fig. 4(a, b), respectively). In addition, the rate capabilities of 8-NE-PP are superior to those of the other samples. At 10, 30, and 50 A g^{-1},
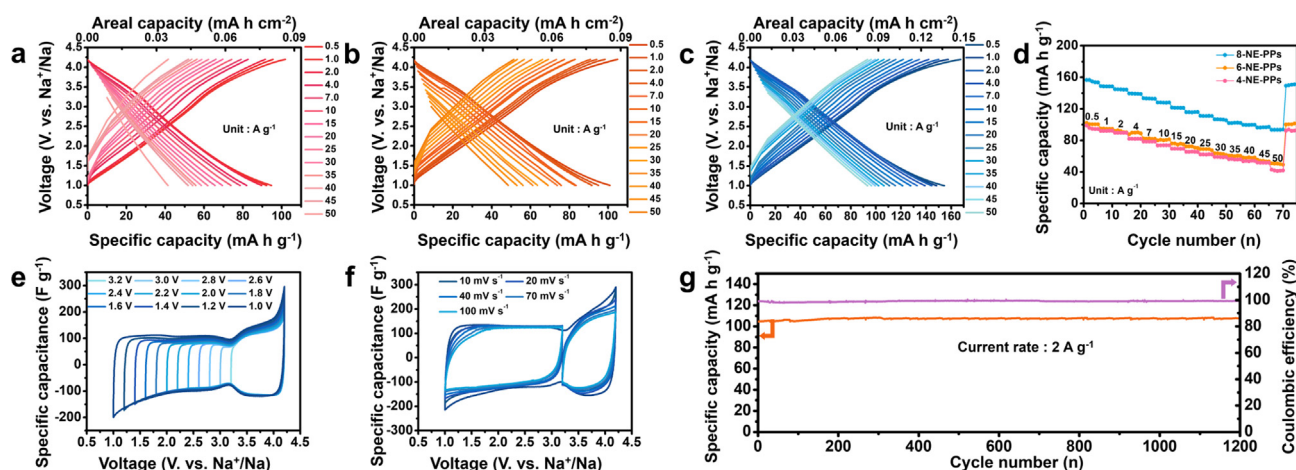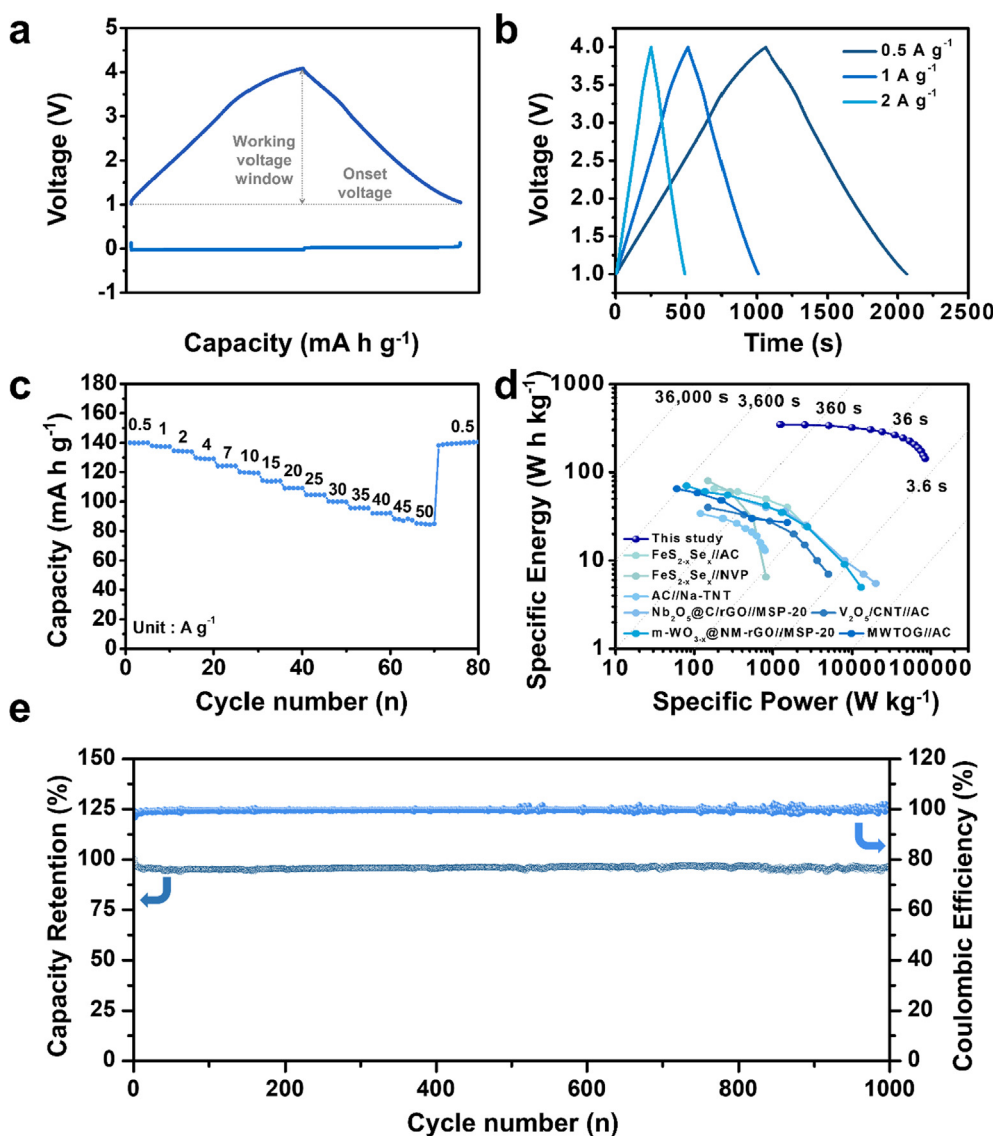
Fig. 4. Electrochemical performances of NE-PPs characterized in the electrolyte of 1 M NaPF$_6$ dissolved in DEGDME in the voltage window of 1.0–4.2 V vs. Na$^+$/Na. Galvanostatic charge/discharge profiles of (a) 4-NE-PP, (b) 6-NE-PP, and (c) 8-NE-PP at different current rates ranging from 0.5 to 50 A g^{-1}, and (d) their rate capabilities. Cyclic voltammograms of 8-NE-PP (e) at different voltages at a scan rate of 5 mV s^{-1} and (f) at different scan rates of 10–100 mV s^{-1} for the two different voltage ranges. (g) Cycling performance of 8-NE-PP over 1200 cycles at 2 A g^{-1}.

values of 128, 107, and 92 mA h g^{-1} were obtained, corresponding to capacity retentions of ~82, ~69, and ~60%, respectively (Fig. 4(d)). For comparison, C-AC was evaluated in the same electrochemical system. As shown in Fig. S15, the microporous C-AC having a low content of mesopores exhibits relatively low capacity and rate capabilities compared with those of all NE-PPs. The highest capacity and rate performance of 8-NE-PP could be attributed to the different pore structure including the few-nanometer pores. The Na-ion–DEGDME complexes are considerably larger than the Na ion, which can limit their adsorption/desorption behaviors in ultramicropores (< 0.7 nm). Therefore, 8-NE-PP with the larger pore size could exhibit a considerably larger effective active surface area than those of the other samples, enabling more accessible charges on the active carbon surface (Table 1). Meanwhile, the charge/discharge profiles exhibit a linear-increase tendency of the initial charge/discharge points, which originates from the ohmic drop with the increasing current rate. The linear relationship between the ohmic drop and current rate suggests that the charge-storage mechanism is based on capacitive behavior. Further specific electrochemical tests were performed for 8-NE-PP. The cyclic voltammograms of 8-NE-PP in different voltage ranges show capacitive charge storage behaviors without voltage hysteresis, indicating a slight pseudocapacitive charge storage behavior (Fig. 4(e)). In addition, the specific capacitances in the voltage range of 1.0–3.2 V (cation charge carriers) are smaller than those in the voltage range of 3.2–4.2 V with anion charge carriers (Fig. 4(e)). This suggests that the Na-ion–DEGDME complex is larger than the anion because the anion is slightly solvated by solvent molecules [46]. With the increase in scan rate, the cation- and anion-derived specific capacitances are slightly changed, indicating a high rate performance (Fig. 4(f)). To examine the charge-storage mechanism of the 8-NE-PPs, an *in situ* impedance spectroscopy analysis was conducted for the second discharge/charge cycle (Fig. S16). The Nyquist plots for different charge states exhibited similar shapes, with a solution resistance (R_s) of ~3 Ω and one small semicircle corresponding to a charge-transfer resistance (R_{ct}) of ~5 Ω, followed by a linear-increase section. The equivalent series resistance values of the Nyquist plots were < 10 Ω. These results indicate that the charge-storage behaviors of the 8-NE-PPs were based on a capacitive mechanism involving the physical adsorption/desorption of charges. For comparison, the charge storage behaviors of 8-NE-PP were also evaluated in a different electrolyte system, 1 M of NaPF$_6$ dissolved in a mixture solvent of ethylene carbonate (EC) and diethyl carbonate (DEC) (1:1 v:v) (Fig. S17). In the voltage window of 1.0–4.2 V vs. Na$^+$/Na, a relatively high specific capacity of ~235 mA h g^{-1} was observed at 0.1 A g^{-1}, while the rate capabilities were inferior to those in the DEGDME-based

electrolyte (Fig. S17(a, b)). This could be attributed to the slow kinetics of the pseudocapacitive charge storage in the carbonate-based electrolyte. In a cycling test, the Faradic reaction causes a gradual capacity fading, yielding a capacity retention of ~65% after 300 cycles (Fig. S17(c)). In contrast, in the DEGDME-based electrolyte, 8-NE-PP exhibits a highly stable cycling behavior, maintaining its initial capacity after 1200 cycles (Fig. 4(g)). Additionally, effects of mass loading densities on the electrochemical performances of 8-NE-PPs were tested by preparing 2 and 4 times higher mass loading samples (2 and 4 mg cm^{-2}). With an increase in the mass loading density, the specific capacities of 8-NE-PPs decreased by ~78 and ~55% for 2 and 4 mg cm^{-2}, respectively, which could be due to the increase in ohmic drop induced by thicker active material packing (Fig. S18). Because the scale-up technologies with high active mass loading are an important issue for the feasible application, future research should focus on the mass loading effects.

SMHCs were fabricated using the pair of NE-P-CL- and NE-PP-based electrodes as anode and cathode, respectively. The electrode was pre-cycled with sodium metal as a half-cell configuration for 20 cycles, which was then disassembled from the half-cell and reassembled as a full cell. The precycling of NE-PP-based cathode was conducted for two important purposes, which were improvement of CE values and charge injection for tuning onset potential. Using excessive sodium metal as an anode is helpful in terms of cycling behaviors because the excessive metal can compensate consumed sodium ions in electrolyte during a long-term cycling process. In contrast, the large amount of sodium metal decreases specific energy density of the full cell device because it is calculated by dividing the weight of all the components including the metal anode. Therefore, in order to reduce metal contents in anode part, high CE performances should be attained in both anode and cathode. As shown in Fig. 4(c), 8-NE-PP-based cathode shows not enough CEs in the initial cycling behaviors, which is settled by precycling over 20 cycles. The mass balance between the anode and the cathode is one of the most important factors in SMHCs. We tested several SMHCs with various mass loading contents in SMA. With the increasing so-diated metal content, the total weight of the SMHCs increased, reducing the specific energy and power densities, as shown in Fig. S19. In contrast, an insufficient amount of SMA did not ensure a long cycle life. Therefore, the proper presodiated sodium metal content is crucial for achieving high electrochemical performance of SMHCs. Accordingly, in the precycling, sodium metal plating (sodiation) was carried out on the NE-P-CL anode to a specific capacity of 80% of that of the cathode. The active mass of the NE-P-CL anode was calculated including the deposited sodium metal. The precycling process can be an efficient

Fig. 5. Electrochemical performances of the SMHC consisting of the precycled NE-P-CL-based anode and NE-PP-based cathode in the voltage window of 1.0–4.0. (a) Schematic of the voltage profiles of both NE-P-CL-based anode and NE-PP-based cathode in the full cell system, (b) galvanostatic charge/discharge profiles at 0.5, 1.0, and 2.0 A g^{-1}, (c) rate capabilities of the SMHC in the current range of 0.5–50 A g^{-1}, (d) Ragone plots of several energy storage devices including the SMHC, and (e) cycling behaviors of the SMHC (capacity retention and CE) over 1000 cycles at 2 A g^{-1}.

method to inject sodium metal and to improve the CE value of SMHCs, while the fastidious process is difficult to be applied in commercial fields. Therefore, the alternative presodiation process is needed in the following researches.

The schematic shows the voltage profiles of the NE-P-CL anode and NE-PP cathode in the full-cell SMHC (Fig. 5(a)), where the NE-P-CL anode is operated in the voltage range smaller than 0.1 V, while the NE-PP cathode in the voltage window of 1.0–4.0 V. To secure more stable cycling behaviors, the operating voltage window of 1.0–4.0 V rather than 1.0–4.2 V is used for the full cell system. The onset voltage of the full cell is tuned to 1.0 V by charge injection in the respective precycling processes of anode and cathode, and the full cell is operated in the voltage window of 1.0–4.0 V (Fig. 5(a)). The galvanostatic charge/discharge profiles of the SMHC exhibit an isosceles-triangle-like shape, typical for electrochemical capacitors (Fig. 5(b)). The profiles correspond to the voltage profile in the schematic (Fig. 5(a)). Notably, high rate capabilities of the SMHC are obtained (Fig. 5(c)). As the active anode mass is only below 10%, the full cell exhibits similar electrochemical performances to those of the NE-PP cathode. The initial specific capacity at 0.5 A g^{-1} is ~140 mA h g^{-1}, while those at 20 and 100

times higher current rates are ~120 and ~85 mA h g^{-1}, respectively (Fig. 5(c)). The high rate capabilities of the SMHC indicate its high power performance. The specific power–energy relationships of several energy storage devices including the NE-P-CL//NE-PP SMHC are shown in Fig. 5(d) [4,6,47–50]. The SMHC exhibits a high specific energy of ~347.7 W h kg^{-1} at a high specific power of ~1241.8 W kg^{-1}. The specific power is considerably improved with a slight reduction in specific energy. When the specific power reaches ~35,000 W kg^{-1}, a specific energy of 263.8 W h kg^{-1} is retained. In addition, the maximum specific power of ~85,300 W kg^{-1} is attained at 143.3 W h kg^{-1}. The specific power performances of the SMHC are superior to those of previously reported sodium-based full-cell energy storage devices (Fig. 5(d)). Moreover, the SMHC exhibits a highly stable cycling performance in a repetitive galvanostatic charge/discharge cycling test (Fig. 5(e)). During 1000 cycles, the stable cycling behavior with a CE of almost 100% is well maintained except the early capacity reduction of ~5%. After the 1000 cycles, the highly stable cycling is retained with a specific capacity of ~94% of the initial capacity (Fig. 5(e)).

3. Conclusion

The nanostructured PPs, NE-P-CL and NE-PP, were fabricated using the polymer precursors by the controlled pyrolysis and simple engineering processes as an electrode pair for the SMHC. NE-P-CL was an amorphous-carbon-based thin layer with a stereoscopic topology including a large number of catalytic sites. The NE-P-CL-based anode significantly reduced the sodium metal nucleation overpotential and provided the homogeneous metal deposition as a film-like shape. This improved the CE values in a wide current density range. In particular, a high CE of ~99.95% was achieved at 1.0 mA cm^{-2}. The average CE of ~99.9% was maintained during the 20th–1000th cycles. In contrast, NE-PP had a large surface area of ~2940 m^2 g^{-1}, while its nanopore sizes were mainly ~2 nm. The highly nanoporous NE-PP stored charges by the capacitive mechanism in the DEGDME-based electrolyte, where it exhibited a specific capacity of ~156 mA h g^{-1} at 0.5 A g^{-1}. The capacity of approximately 92 mA h g^{-1} (60% of the initial capacity) was maintained at the 100 times higher current rate, indicating the high rate capability. The high-performance PP-based electrode pair was assembled as Faradic and non-Faradic electrodes in the SMHC after the precycling and presodiation. The SMHC exhibited a very high specific power of ~85,300 W kg^{-1} and high specific energy of ~347.7 W h kg^{-1}. In addition, the very stable cycling behavior was maintained over 1000 cycles with a capacity retention of 94% and CE of almost 100%.

4. Experimental section

4.1. Fabrication of NE-PCL and NE-PPs

For the fabrication of NE-P-CL, PVP (M_w = ~360,000, Sigma-Aldrich) was dissolved in ethanol (2 wt%) under vigorous stirring. The polymer thin film was prepared through the spin coating of polymer solution droplets onto the Cu foil at 4000 rpm for 30 s. The PVP-thin-film-coated Cu foil was then heat-treated in a tubular furnace at 800 °C for 2 h under an Ar gas flow at a rate of 5 °C min^{-1}. After cooling to room temperature, the resulting NE-P-CL was stored in a vacuum oven at 30 °C. For the preparation of NE-PPs, the WGT residue was dried in a convection oven at 30 °C for 3 days. The dried precursor (6 g) was heat-treated in the furnace at 600 °C for 2 h under the Ar gas flow at a heating rate of 5 °C min^{-1}. The pretreated sample (2 g) was then mixed with 400-, 600-, or 800- wt% KOH in a mortar, which was activated in the furnace at 800 °C for 2 h under Ar gas flow. A heating rate of 5 °C min^{-1} was employed in the activation process. The resulting products, NE-PPs, were washed with distilled water and ethanol several times by vacuum filtration and stored in a vacuum oven at 30 °C.

4.2. Characterization

The sample morphologies were observed by FESEM (S-4300SE, Hitachi, Japan) and FETEM (JEM2100F, JEOL, Japan). XRD (Rigaku, DMAX 2500) was carried out using a Cu K$_\alpha$ radiation generator (λ = 0.154 nm) at 40 kV and 100 mA in the 2θ range of 10–60°. The chemical structures of NE-P-CL and NE-PPs were investigated by XPS (PHI 5700 ESCA, Chanhassen, USA) using monochromatic Al K$_\alpha$ radiation. The Raman spectra of NE-P-CL and NE-PPs were acquired using a continuous linearly polarized laser with a wavelength of 514.5 nm and 1200-groove/mm grating. The spot diameter of the Raman laser was approximately 1 nm. A 100× objective lens was used. The pore structures of NE-PPs were calculated using the nitrogen adsorption/desorption isotherms (ASAP 2020, Micromeritics, USA) measured at −196 °C.

4.3. Electrochemical characterization

The electrochemical performances of the bare Cu-foil- and NE-P-CL-based SMAs, C-AC- and NE-PP-based cathodes, and their full SMHCs were analyzed using a Wonatech automatic battery cycler and CR2032-type coin cells. For the half-cell experiments, coin cells were assembled in a glove-box filled with argon using the corresponding material as the working electrode and metallic Na foils as the reference and counter electrodes. NaPF$_6$ (1 M; Sigma-Aldrich, 98%) was dissolved in a solution of DEGDME and used as the electrolyte for the half-cell tests. A glass microfiber filter (Whatman) was used as a separator. The working electrode for the SMA was prepared by mechanically producing a working electrode cylinder having a diameter of 0.5 in. In addition, the working electrode for the capacitive cathode was prepared by mixing the active material (80 wt%) with conductive carbon (10 wt%) and polyvinylidene fluoride (10 wt%) in N-methyl-2-pyrrolidone. The resulting slurry was uniformly introduced onto an Al foil. The electrodes were dried at 120 °C for 2 h and roll-pressed. The loading contents of NE-PPs were ~1 mg cm^{-2}. SMHCs were prepared after the precycling of both NE-P-CL-based anode and NE-PP-based cathode for 20 cycles in corresponding half-cell configurations. In the precycling, sodium metal (approximately 0.1 mg cm^{-2}) was loaded on NE-P-CL and the voltage of NE-PP was tuned to 1.0 V vs. Na$^+$/Na. After assembling the full cell using the precycled electrode pair, we operated the SMHC, which had a total active loading content of ~1.1 mg, in the voltage window of 1.0–4.0 V at different current rates for all the electrochemical characterizations (including its cycling performance). Specific energy density and power density of the full cell were calculated from the galvanostatic discharge profiles by the followed formula: $E_s = n \cdot F \cdot V / W_{total}$ and $P_s = n \cdot F \cdot V / T \cdot W_{total}$, where E, P, F, V, T, n and W_{total} are specific energy density, specific power density, faraday constant, thermodynamic equilibrium voltage, time, number of the charge and total weight of both anode and cathode, respectively.

CRediT authorship contribution statement

Sunwoo Park: Methodology, Investigation, Visualization, Writing - review & editing. **Jong Chan Hyun:** Methodology, Investigation. **Jin Hwan Kwak:** Data curation, Resources. **Min Eui Lee:** Data curation, Resources, Validation. **Hyoung-Joon Jin:** Supervision, Project administration, Funding acquisition. **Young Soo Yun:** Writing - original draft, Conceptualization, Supervision, Project administration.

Declaration of Competing Interest

The authors declare that they have no known competing financial interests or personal relationships that could have appeared to influence the work reported in this paper.

Appendix A. Supplementary data

Supplementary data to this article can be found online at https://doi.org/10.1016/j.apsusc.2020.145848.

References

[1] J. Ding, W. Hu, E. Peak, D. Mitlin, Review of hybrid ion capacitors: From aqueous to lithium to sodium, Chem. Rev. 118 (2018) 6457–6498, https://doi.org/10.1021/acs.chemrev.8b00116.

[2] B. Li, J. Zheng, H. Zhang, L. Jin, D. Yang, H. Lv, C. Shen, A. Shellikeri, Y. Zheng, R. Gong, J.P. Zheng, C. Zhang, Electrode materials, electrolytes, and challenges in nonaqueous lithium-ion capacitors, Adv. Mater. 30 (2018) 1705670, https://doi.org/10.1002/adma.201705670.

[3] X.-Y. Shan, Y. Wang, D.-W. Wang, F. Li, H.-M. Cheng, Armoring graphene cathodes for high-rate and long-life lithium ion supercapacitors, Adv. Energy Mater. 6 (2016) 1502064, https://doi.org/10.1002/aenm.201502064.

[4] E. Lim, C. Jo, M.S. Kim, M.-H. Kim, J. Chun, H. Kim, J. Park, K.C. Roh, K. Kang, S. Yoon, J. Lee, High-performance sodium-ion hybrid supercapacitor based on Nb₂O₅@carbon core-shell nanoparticles and reduced graphene oxide nanocomposites, Adv. Funct. Mater. 26 (2016) 3711–3719, https://doi.org/10.1002/adfm.201670130.

[5] H. Kim, M.-Y. Cho, M.-H. Kim, K.-Y. Park, H. Gwon, Y. Lee, K.C. Roh, K. Kang, A novel high-energy hybrid supercapacitor with an anatase TiO₂-reduced graphene oxide anode and an activated carbon cathode, Adv. Energy Mater. 3 (2013) 1500–1506, https://doi.org/10.1002/aenm.201300467.

[6] Z. Le, F. Liu, P. Nie, X. Li, X. Liu, Z. Bian, G. Chen, H.B. Wu, Y. Lu, Pseudocapacitive sodium storage in mesoporous single-crystal-like TiO₂-graphene nanocomposite enables high-performance sodium-ion capacitors, ACS Nano 11 (2017) 2952–2960, https://doi.org/10.1021/acsnano.6b08332.

[7] M. Wang, Y. Zhong, J. Ren, X. Zhou, J. Wei, Z. Zhou, S. Jin, Fabrication of high-power Li-ion hybrid supercapacitors by enhancing the exterior surface charge storage, Adv. Energy Mater. 5 (2015) 1500550, https://doi.org/10.1002/aenm.201500550.

[8] H. Wang, C. Guan, X. Wang, H.J. Fan, A high energy and power Li-ion capacitor based on a TiO2 nanobelt array anode and a graphene hydrogel cathode, Small 11 (2015) 1470–1477, https://doi.org/10.1002/smll.201402620.

[9] V. Aravindan, D. Mhamane, W.C. Ling, S. Ogale, S. Madhavi, Nonaqueous lithium-ion capacitors with high energy densities using trigol-reduced graphene oxide nanosheets as cathode-active material, ChemSunChem 6 (2013) 2240–2244, https://doi.org/10.1002/cssc.201300465.

[10] M.Y. Song, N.R. Kim, H.J. Yoon, S.Y. Cho, H.-J. Jin, Y.S. Yun, Long-lasting Nb₂O₅-based nanocomposite materials for Li-ion storage, ACS Appl. Mater. Interfaces 9 (2017) 2267–2274, https://doi.org/10.1021/acsami.6b11444.

[11] S. Taminato, M. Yonemura, S. Shiotani, T. Kamiyama, S. Torii, M. Nagao, Y. Ishikawa, K. Mori, T. Fukunaga, Y. Onodera, T. Naka, M. Morishima, Y. Ukyo, D.S. Adipranoto, H. Arai, Y. Uchimoto, Z. Ogumi, K. Suzuki, M. Hirayama, R. Kanno, Real-time observations of lithium battery reactions-operando neutron diffraction analysis during practical operation, Sci. Pep 6 (2016) 28843, https://doi.org/10.1038/srep28843.

[12] T. Drezen, N.-H. Kwon, P. Bowen, I. Teerlinck, M. Isono, I. Exnar, Effect of particle size on LiMnPO₄ cathodes, J. Power Sources 174 (2007) 949–953, https://doi.org/10.1016/j.jpowsour.2007.06.203.

[13] P. Simon, Y. Gogotsi, B. Dunn, Where do batteries end and supercapacitors begin? Science 343 (2014) 1210–1211, https://doi.org/10.1126/scnience.1249625.

[14] M. Okubo, E. Hosono, J. Kim, M. Enomoto, N. Kojima, T. Kudo, H. Zhou, I. Honma, Nanosize effect on high-rate Li-ion intercalation in LiCoO₂ electrode, J. Am. Chem. Soc. 120 (2007) 7444–7452, https://doi.org/10.1021/ja0681927.

[15] A.S. Arico, P. Bruce, B. Scrosati, J.-M. Tarascon, W.V. Schalkwijk, Nanostructured materials for advanced energy conversion and storage devices, Nat. Mater. 4 (2005) 366–377, https://doi.org/10.1038/nmat1368.

[16] C. Chen, Y. Wen, X. Hu, X. Ji, M. Yan, L. Mai, P. Hu, B. Shan, Y. Huang, Na⁺ intercalation pseudocapacitance in graphene-coupled titanium oxide enabling ultra-fast sodium storage and long-term cycling, Nat. Commun. 6 (2015) 6929, https://doi.org/10.1038/ncomms7929.

[17] T. Ling, P. Da, X. Zheng, B. Ge, Z. Hu, M. Wu, X.-W. Du, W.-B. Hu, M. Jaroniec, S.-Z. Qiao, Atomic-level structure engineering of metal oxides for high-rate oxygen intercalation pseudocapacitance, Sci. Adv. 4 (2018) eaau6261, https://doi.org/10.1126/sciadv.aau6261.

[18] H. Kim, K. Lim, G. Yoon, J.-H. Park, K. Ku, H-D. Lim, Y.-E. Sung, K. Kang, Exploiting lithium-ether co-intercalation in graphite for high-power lithium-ion batteries, Adv Energy Mater. 7 (2017) 1700418, https://doi.org/10.1002/aenm.201700418.

[19] Se Youn Cho, Minjee Kang, Jaewon Choi, Min Eui Lee, Hyeon Ji Yoon, Hae Jin Kim, Cecilia Leal, Sungho Lee, Hyoung-Joon Jin, Young Soo Yun, Pyrolytic carbon nanosheets for ultrafast and ultrastable sodium-ion storage, Small 14 (17) (2018) 1703043, https://doi.org/10.1002/smll.20170304310.1002/smll.201703043.

[20] Z.W. Seh, J. Sun, Y. Sun, Y. Cui, A Highly reversible room-temperature sodium metal anode, ACS Central Sci. 1 (2015) 449–455, https://doi.org/10.1021/acscentsci.5b00328.

[21] A.P. Cohn, N. Muralidharan, R. Carter, K. Share, C.L. Pint, Anode-free sodium battery through in situ plating of sodium metal, Nano Lett. 17 (2017) 1296–1301, https://doi.org/10.1021/acs.nanolett.6b05174.

[22] Y. Zhao, L.V. Goncharova, A. Lushington, Q. Sun, H. Yadegari, B. Wang, W. Xiao, R. Li, X. Sun, Superior stable and long life sodium metal anodes achieved by atomic layer deposition, Adv. Mater 29 (2017) 1606663, https://doi.org/10.1002/adma.201606663.

[23] H.J. Yoon, N.R. Kim, H.-J. Jin, Y.S. Yun, Macroporous catalytic carbon nanotemplates for sodium metal anodes, Adv Energy Mater. 8 (2018) 1701261, https://doi.org/10.1002/aenm.201701261.

[24] J. Song, G. Jeong, A.-J. Lee, J.H. Park, H. Kim, Y.-J. Kim, Dendrite-free polygonal sodium deposition with excellent interfacial stability in a NaAlCl₄ − 2SO₂ inorganic electrolyte, ACS Appl. Mater. Interfaces 7 (2015) 27206–27214, https://doi.org/10.1021/acsami.5b08111.

[25] W. Luo, C-F. Lin, O. Zhao, M. Noked, Y. Zhang, G.W. Rubloff, L. Hu, Ultrathin surface coating enables the stable sodium metal anode, Adv. Energy Mater. 7 (2017) 1601526, https://doi.org/10.1002/aenm.201601526.

[26] R. Cao, K. Mishra, X. Li, J. Qian, M.H. Engelhard, M.E. Bowden, K.S. Han, K.T. Mueller, W.A. Henderson, J.-G. Zhang, Enabling room temperature sodium metal batteries, Nano Energy 30 (2016) 825–830, https://doi.org/10.1016/j.nanoen.2016.09.013.

[27] J. Lee, Y. Lee, J. Lee, S.-M. Lee, J.-H. Choi, H. Kim, M.-S. Kwon, K. Kang, K.T. Lee, N.-S. Choi, Ultraconcentrated sodium bis(fluorosulfonyl)imide-based electrolytes for high-performance sodium metal batteries, ACS Appl. Mater. Interfaces 9 (2017) 3723–3732, https://doi.org/10.1021/acsami.6b14878.

[28] Y.-J. Kim, H. Lee, H. Noh, J. Lee, S. Kim, M.-H. Ryou, Y.M. Lee, H.-T. Kim, Enhancing the cycling stability of sodium metal electrodes by building an inorganic-oragnic composite protective layer, ACS Appl. Mater. Interfaces 9 (2017) 6000–6006, https://doi.org/10.1021/acsami.6b14437.

[29] Min Eui Lee, Seunggon Lee, Jaewon Choi, Hyoung-Joon Jin, Seungyong Han, Young Soo Yun, Anode-free sodium metal batteries based on nanohybrid core–shell templates, Small 15 (37) (2019) 1901274, https://doi.org/10.1002/smll.v15.3710.1002/smll.201901274.

[30] A. Wang, X. Hu, H. Tang, C. Zhang, S. Liu, Y.-W. Yang, Q.-H. Yang, J. Luo, Processable and moldable sodium-metal anodes, Angew. Chem. Int. Ed. 56 (2017) 11921–11926, https://doi.org/10.1002/anie.201703937.

[31] N.R. Kim, S.M. Lee, M.W. Kim, H.J. Yoon, W.G. Hong, H.J. Kim, H.J. Choi, H.-J. Jin, Y.S. Yun, Amphicharge-storable pyropolymers containing multitiered nanopores, Adv. Energy Mater. 7 (2017) 1700629, https://doi.org/10.1002/aenm.201700629.

[32] S.Y. Cho, H.J. Yoon, N.R. Kim, Y.S. Yun, H.-J. Jin, Sodium-ion supercapacitors based on nanoporous pyroproteins containing redox-active heteroatoms, J. Power Sources 329 (2016) 536–545, https://doi.org/10.1016/j.jpowsour.2016.08.114.

[33] H.J. Yoon, M.E. Lee, N.R. Kim, S.J. Yang, H.-J. Jin, Y.S. Yun, Hierarchically nanoporous pyropolymer nanofibers for surface-induced sodium-ion storage, Electrochim. Acta 242 (2017) 38–46, https://doi.org/10.1016/j.electacta.2017.05.014.

[34] Y. Yamada, Y. Takazawa, K. Miyazaki, T. Abe, Electrochemical lithium intercalation into graphite in dimethyl sulfoxide-based electrolytes: effect of solvation structure of lithium ion, J. Phys. Chem. C 114 (2010) 11680–11685, https://doi.org/10.1021/jp1037427.

[35] T. Abe, N. Kawabata, Y. Mizutani, M. Inaba, Z. Ogumi, Correlation between cointercalation of solvents and electrochemical intercalation of lithium into graphite in propylene carbonate solution, J. Electrochem. Soc. 150 (2003) A257–A261, https://doi.org/10.1149/1.1541004.

[36] G. Yoon, H. Kim, I. Park, K. Kang, Conditions for reversible Na intercalation in graphite: theoretical studies on the interplay among guest ions, solvent, and graphite Host, Adv. Energy Mater. 7 (2016) 1601519, https://doi.org/10.1002/aenm.201601519.

[37] S.Y. Cho, Y.S. Yun, D. Jang, J.W. Jeon, B.H. Kim, S. Lee, H.-J. Jin, Ultra strong pyroprotein fibres with long-range ordering, Nat. Commun. 8 (2017) 74, https://doi.org/10.1038/s41467-017-00132-3.

[38] R. Zhang, X.-R. Chen, X. Chen, X.-B. Cheng, X.-Q. Zhang, C. Yan, Q. Zhang, Lithiophilic sites in doped graphene guide uniform lithium nucleation for dendrite-free lithium metal anodes, Angew. Chem. Int. Ed. 56 (2017) 7764–7768, https://doi.org/10.1002/anie.201702099.

[39] Y.S. Yun, S.Y. Cho, H. Kim, H.-J. Jin, K. Kang, Ultra-thin hollow carbon nanospheres for pseudocapacitive sodium-ion storage, ChemElectroChem 2 (2015) 359–365, https://doi.org/10.1002/celc.201402359.

[40] H.-G. Wang, Z. Wu, F.-I. Meng, D.-I. Ma, X.-I. Huang, L.-M. Wang, X.-B. Zhang, Nitrogen-doped porous carbon nanosheets as low-cost, high-performance anode material for sodium-ion batteries, ChemSusChem 6 (2013) 56–60, https://doi.org/10.1002/cssc.201200680.

[41] W. Plieth, Electrochemistry for Materials Science, Elsevier, Amsterdam, 2008.

[42] D.R. Ely, R.E. Garcia, Heterogeneous nucleation and growth of lithium electrodeposits on negative electrodes, J. Electrochem. Soc. 160 (2013) A662–A668, https://doi.org/10.1149/1.057304jes.

[43] A. Pei, G. Zheng, F. Shi, Y. Li, Y. Cui, Nanoscale nucleation and growth of electrodeposited lithium metal, Nano Lett. 17 (2017) 1132–1139, https://doi.org/10.1021/acs.nanolett.6b04755.

[44] G. Li, Z. Liu, Q. Huang, Y. Gao, M. Regula, D. Wang, L.-Q. Chen, D. Wang, Stable metal battery anodes enabled by polyethylenimine sponge hosts by way of electrokinetic effects, Nat. Energy 3 (2018) 1076–1083, https://doi.org/10.1038/s41560-018-0276-z.

[45] G. Li, Z. Liu, D. Wang, X. He, S. Liu, Y. Gao, A. AlZahrani, S.H. Kim, L.-Q. Chen, D. Wang, Electrokinetic phenomena enhanced lithium-ion transport in leaky film for stable lithium metal anodes, Adv. Energy Mater. 9 (2019) 1900704, https://doi.org/10.1002/aenm.201900704.

[46] Kang Xu, Electrolytes and interphases in Li-Ion batteries and beyond, Chem. Rev. 114 (23) (2014) 11503–11618, https://doi.org/10.1021/cr500003w.

[47] Yaqiong Long, Jing Yang, Xin Gao, Xuena Xu, Weiliu Fan, Jian Yang, Shifeng Hou, Yitai Qian, Solid-solution anion-enhanced electrochemical performances of metal sulfides/selenides for sodium-ion capacitors: The case of FeS₂₋ₓSeₓ, ACS Appl. Mater. Interfaces 10 (13) (2018) 10945–10954, https://doi.org/10.1021/acsami.8b00931.

[48] J. Yin, L. Qi, H. Wang, Sodium titanate nanotubes as negative electrode materials for sodium-ion capacitors, ACS. Appl. Mater. Interfaces 4 (2012) 2762–2768, https://doi.org/10.1021/am300385r.

[49] Z. Chen, V. Augustyn, X. Jia, Q. Xiao, B. Dunn, Y. Lu, High-performance sodium-ion pseudocapacitors based on hierarchically porous nanowire composites, ACS Nano 6 (2012) 4319–4327, https://doi.org/10.1021/nn300920e.

[50] M.S. Kim, E. Lim, S. Kim, C. Jo, J. Chun, J. Lee, General synthesis of N-doped marcroporous graphene-encapsulated mesoporous metal oxides and their application as new anode materials for sodium-ion hybrid supercapacitors, Adv. Funct. Mater. 27 (2017) 1603921, https://doi.org/10.1002/adfm.201603921.